Synergistic effect of Fe/Co-doping and electric field in Niobium Diboride for boosting hydrogen production

Khossossi, Nabil; Banerjee, Amitava; Dey, Poulumi

DOI
10.1016/j.surfin.2023.102972

Publication date
2023

Document Version
Final published version

Published in
Surfaces and Interfaces

Citation (APA)
Khossossi, N., Banerjee, A., & Dey, P. (2023). Synergistic effect of Fe/Co-doping and electric field in Niobium Diboride for boosting hydrogen production. *Surfaces and Interfaces*, *39*, Article 102972. https://doi.org/10.1016/j.surfin.2023.102972

Surfaces and Interfaces 39 (2023) 102972

Contents lists available at ScienceDirect

Surfaces and Interfaces

journal homepage: www.sciencedirect.com/journal/surfaces-and-interfaces

Synergistic effect of Fe/Co-doping and electric field in Niobium Diboride for boosting hydrogen production

Nabil Khossossi [a,*], Amitava Banerjee [b], Poulumi Dey [a,*]

[a] *Department of Materials Science and Engineering, Faculty of Mechanical, Maritime and Materials Engineering, Delft University of Technology, Mekelweg 2, Delft, 2628 CD, The Netherlands*
[b] *Department of Metallurgical and Materials Engineering, Indian Institute of Technology, Jodhpur, Rajasthan 342030, India*

ARTICLE INFO

Keywords:
Catalytic activity
Thermodynamic properties
Electrocatalysts
Evolution reactions
Transitional metal Diboride

ABSTRACT

A primary concern towards achieving a robust and sustainable water-splitting strategy consists in the development and designing of non-precious hydrogen evolution electrocatalysts capable of operating at relatively high current densities. In the present density functional theory (DFT) based study, we explored and identified α-NbB_2-based catalysts consisting of Borophene as graphene-like noble metal-free networks in Niobium-metal based networks, as promising catalysts for the hydrogen-evolution reaction (HER). Our results unveiled that Fe/Co covalent doping in α-NbB_2 $\{001\}$ surface provides high-efficiency HER activity sites, namely, T_{Nb}-sites in Nb-terminated Fe/Co-NbB_2 $\{001\}$ surface with the lowest ΔG_{H^*} Gibbs free energy value of about 0.264/0.278 eV, which further drops to a very optimal value in the range of $\Delta G_{H^*} \leq \pm 0.10$ eV upon the implementation of an external electric field. Furthermore, it was also revealed that in contrast to the extensively used Pt-based surface catalysts, both α-NbB_2 and Fe/Co-NbB_2 catalysts can sustain consistently high catalytic activity for HER over a very large hydrogen coverage and thus ensure a large density of effective catalytic free sites.

1. Introduction

In recent years, the growing concerns about global warming and carbon footprint have urged researchers to investigate the possibility of green energy. Hydrogen, as a clean and sustainable energy carrier, has attracted considerable attention due to its high gravimetric energy density, and it could be a promising alternative to traditional fuels. However, hydrogen energy faces several bottlenecks, such as production and storage [1–4]. Hydrogen production by water splitting has become a promising strategy to convert the large excess amount of electrical energy from renewable energy resources to the form of a clean fuel—hydrogen (H_2). Clean fuel, because it produces only water as a byproduct when H_2 is used as a fuel in fuel cell-based engines. So, there is a global drive towards the development of the water-splitting technique for hydrogen production [5,6]. In this context, the development of efficient and cost-effective catalysts for water-splitting has become a significant challenge. Therefore, the design of novel and efficient catalysts is essential to enable sustainable hydrogen production and storage, thus contributing to the development of a sustainable energy system.

Electrocatalytic water splitting, $2H_2O \rightarrow 2H_2 + O_2$, is usually carried out in either acidic or alkaline media [7]. During this process, the two half-reactions can be expressed in different ways [7]. Due to the sluggish kinetics of both hydrogen evolution reaction (HER) and oxygen evolution reaction (OER), the electrocatalytic efficiency of the actual water splitting is limited by the high operating voltage (1.8–2.0 V), which is much larger than the theoretical minimum value of 1.23 V [8]. The optimum catalysts for HER and OER require the lowering of overpotential associated with these reactions. At present, we get more than approximately 5% of the world's hydrogen through this water-splitting process generating hydrogen and oxygen, which needs substantial improvement [9]. Transition metal-based catalysts have mostly drawn significant attention, out of various other catalysts such as precious metal-free catalysts for water splitting [5,6,10–12]. Unfortunately, the solar-to-hydrogen conversion efficiency remains low though many strategies, including structural and defect engineering, plasmonic effects, and elemental doping, have been discussed to improve catalysts' optical absorption and photo-induced charge separation and transport, etc [13–16].

In this work, we are focusing on a member of transitional metal borides (TMBs), NbB_2-based catalysts for hydrogen evolution reaction. As it is known, the electronic states of transition metals mostly depend on their coordination environment. In general, the transition metals coordinating with atoms composed of highly electronegative O, S, and *N* could easily lead to a highly oxidized state, which probably decreases

---

* Corresponding authors.
E-mail addresses: n.khossossi@tudelft.nl (N. Khossossi), p.dey@tudelft.nl (P. Dey).

https://doi.org/10.1016/j.surfin.2023.102972
Received 27 February 2023; Received in revised form 5 May 2023; Accepted 15 May 2023

the number of active sites [17]. TMBs have drawn our attention due to their fascinating properties, including good chemical stability, high thermal and electrical conductivities, as well as a variety of technological applications, such as metal-air batteries, CO_2 conversion, and catalysis [18–23]. It is reported that transition metal and boron coordination results in partial electron transfer from B to the vacant d-orbital of the transition metals, making the transition metals electron-rich and the boron an electron-deficient center [24]. This electron-deficient center can protect the transition metal from oxidation and preserve the active species. We have previously explored 2D boron, i.e., borophene with and without transition metal, as a bifunctional catalyst for water splitting [7].

Herein, we have investigated the catalytic properties of the Niobium Diboride α-NbB_2 {001} surface, which has been previously synthesized and observed to be preferentially exposed in α-NbB_2 thin films [25]. The {001} plane was selected as it is the most stable and commonly studied surface of α-NbB_2, with a well-defined crystallographic orientation. We further examined the effect of doping with Iron (Fe) and Cobalt (Co) on the hydrogen evolution reaction. We found that the Fe/Co covalent doping can effectively tune the surface charge redistribution of α-NbB_2 {001} surface, thus lowering the Gibbs free energy to about 0.264/0.278 eV thereby facilitating the HER thermodynamic performance. Additionally, we observed that the synergetic effect of an external transverse electric field and Fe/Co doping can advantageously boost the HER activity, with a Gibbs free energy of H* binding reaching the catalyst's optimal values of $\Delta G^*_H \leq \pm$ 0.10 eV. Furthermore, we demonstrated that in contrast to the broadly studied Pt{111} catalysts, the α-NbB_2 based catalysts can maintain and even increase the catalytic activity for HER over a range of considerable hydrogen concentration.

2. Theoretical details

2.1. Mechanism and gibbs free energy of HER

HER is a conventional electrochemical half-cell reaction involving the reduction of protons to hydrogen [26]. The HER is mainly performed in acidic media by using Platinum (Pt) as catalyst material or in alkaline media by using less noble metals such as Nickel (Ni). H^+-adsorption on the hydrogen evolution catalyst surface is the first step, known as Volmer step, followed by Heyrovsky or Tafel steps. In this context, the HER can occur through the three following elementary reaction pathways:

$$\textbf{Volmer}: \quad H^+(aq) + e^- + * \rightarrow H^* \tag{1}$$

$$\textbf{Tafel}: \quad 2H^* \rightarrow H_2(g) + 2* \tag{2}$$

$$\textbf{Heyrovsky}: \quad H^* + e^- + H^+ \rightarrow H_2(g) + * \tag{3}$$

wherein the asterisk (*) designates an active site on the catalyst surface and H* designates hydrogen atom adsorbed on the catalyst surface. The initial step in the HER is the Volmer process, in which a H^+-e^- pair forms an adsorbed H-atom on the catalyst surface. During the second step of the HER reaction, the H_2 molecule is produced by either the Tafel or Heyrovsky reaction or both. In the case of Tafel reaction (Eq. (2)), two adsorbed hydrogen atoms scatter initially on the catalyst surface and then form a H_2 molecule by interacting. While in the case of Heyrovsky reaction, (Eq. (3)), a H^+ arising from the electrolyte adsorbs directly onto a hydrogen atom already adsorbed on the catalyst surface and is then reduced to form a H_2 molecule. Nevertheless, the mechanism that dominates the adsorption process has proven to be complex to elucidate [27]. Although this difficulty in understanding the HER of all these reactions, it has been established that the adsorbed hydrogen, H*, is the unique intermediate species in the whole process. Furthermore, it is essential to note that a suitable HER catalyst always binds H^+ very fast and releases the product. Hence, the electrochemical HER facilitates the production of H_2 on a large scale.

In order to determine the suitable candidate catalyst for HER, it is necessary to calculate the adsorption energy of the hydrogen atom on the catalyst surface. The adsorption energy is linked to the Gibbs free energy according to the equation:

$$\Delta G_{H^*} = \Delta E_{H^*} + \Delta E_{ZPE} - T\Delta S, \tag{4}$$

where the adsorption of neutral hydrogen is undertaken on a specific catalyst surface site, ΔE_{H^*} refers to the binding energy calculated for intermediate hydrogen adsorbed on the surface of the catalyst, as described below:

$$\Delta E_{H^*} = (E_{nH^*} - E_{(n-1)H^*} - \frac{1}{2}E_{H_2}), \quad n \geq 1 \tag{5}$$

where E_{nH^*} denotes the total energy with n hydrogen atom adsorbed on the catalyst surface, $E_{(n-1)H^*}$ is the total free energy of n-1 hydrogen coverage system and E_{H_2} is the gas-phase energy of H_2 molecule. In the Eq. (4), ΔE_{ZPE} refers to the difference in zero-point energies correction and has been computed to be 0.04 eV. The ΔS defines the difference in entropy between the adsorbed hydrogen and the gas phase and can be determined approximately as the entropy of H_2 gas at normal conditions of temperature (T) and pressure (P), as shown below:

$$\Delta S = (S_H - \frac{1}{2}S_{H_2}) \approx -\frac{1}{2}S^0_{H_2} \tag{6}$$

2.2. Density functional theory calculations

All the calculations have been conducted through first-principles calculations as implemented in the Vienna ab-initio simulation package (VASP) [28]. Generalized Gradient Approximation (GGA) in the form of Perdew–Burke–Ernzerhof functional (PBE) has been employed for an exchange–correlation interaction [29]. The van der Waals interactions with DFT-D3 were assessed by Grimme et al. [30]. The hydrogen activity was explored on two distinct Nb- and B-terminated {001} surface of α-NbB_2 and Fe/Co covalent doped α-NbB_2 modeled via a periodic super-cell slab. For the plane-wave basis set, an energy cutoff of 500 eV and (7 × 7 × 1) k-meshes for (2 × 2 × 1) super-cell for Brillouin zone integration within the Monkhorst–Pack scheme was chosen [31]. To describe the ion-electron interaction, we have used the Projected augmented wave (PAW) method [32]. In addition, a vacuum of 20 Å has been used in the transverse directions to prevent any interactions between the consecutive layers.

3. Results and discussion

3.1. Characterization of Niobium Diboride α-NbB_2

α-NbB_2 bulk was identified and synthesized in a hexagonal lattice structure that belongs to the space group P6/mmm with the number 191 [33–35]. As depicted in Fig. 1(a-b), the α-NbB_2 lattice structure can be viewed as an interconnected "sandwich" configuration made by embedding Boron monolayers in Niobium-metal based networks forming three types of bonds, namely: (i) covalent B–B bonds in the graphene-like boron sheets, (ii) metallic Nb–Nb and (iii) ionic Nb–B bonds. Thus, the Niobium-atoms exhibit metallic bonding within 3D frameworks, while the Boron-atoms exhibit covalent bonding within uncommon two-dimensional graphene-like Borophene nanosheets which is not an isolated stable lattice phase. The computed lattice parameters are a = b = 3.118 Å and c = 3.337 Å in good agreement with prior theoretical and experimental values (a = b = 3.115 and c = 3.265 Å) [36,37], the length of B–B bond in the Boron layer of α-NbB_2 is about 1.801 Å slightly similar than the length of B–B bond in 2D Borophene nanosheets. Also, the length of the Nb–Nb bond within the Nb metal structure is found to be 3.118 Å, which is in line with the Nb–Nb bond length (3.12 Å) within the Niobium structured in the hexagonal space group. The present finding states that upon deleting the B atoms in α-NbB_2, all the remaining Niobium atoms can be incorporated into a 3D metal structure. Accordingly, the α-NbB_2 structure can be characterized as

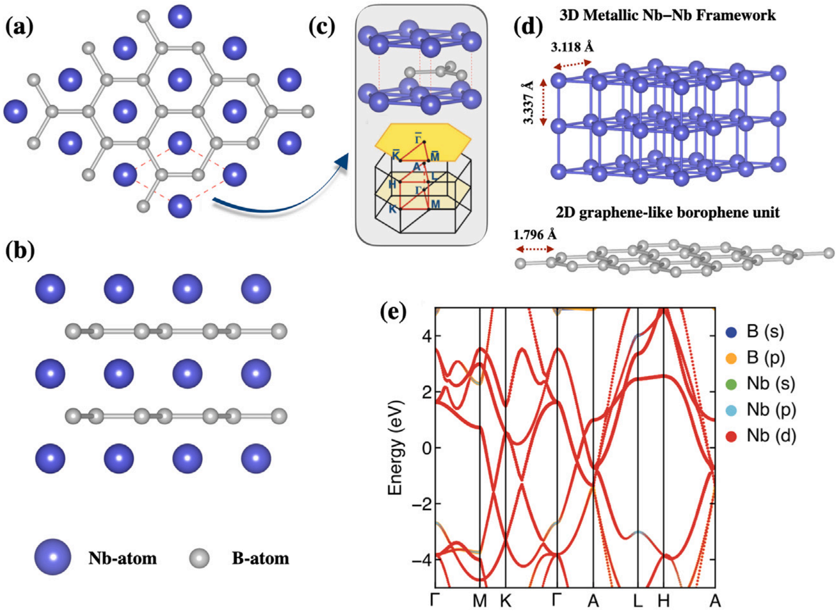

Fig. 1. (a–b) Schematic illustration of bulk Niobium Diboride α-NbB_2 (P6/mmm, no 191) crystal. The unit cell is indicated by the red dashed line. (c) Irreducible Brillouin Zone along with the high symmetry points, (d) 3D metallic Nb–Nb framework and 2D graphene-like borophene unit in α-NbB_2, and (e) The calculated projected band structures. The energy at the Fermi level was set to zero. (For interpretation of the references to color in this figure legend, the reader is referred to the web version of this article.)

an inter-connected sandwich-like pattern consisting of graphene-like borophene nanosheets embedded in Niobium-based 3D networks as illustrated in Fig. 1(d).

Additionally, the computed projected electronic band structure of the diboride α-NbB_2 is displayed in Fig. 1(e), where quasi-degenerate states having low effective masses can be noticed close to the Fermi-level, particularly, the band crossing along the A-point, together with states close to the K-point. The diboride α-NbB_2 is conductive and endowed with metallic characteristics, thereby evincing that its Fermi-level is crossed by the band lines derived from both 3D Nb-metal structure and borophene sheets. Previous experimental reports reveal that out of all the Nb–B based compounds, α-NbB_2 was deemed as a prospective Ultra High-Temperature Composite (UHTC) for high-temperature structural purposes owing to its unique mixture of proprieties including high thermal conductivity (17–23.5 W/m K), electrical conductivity (1.54×10^6 S/m) and excellent chemical stability [25, 38–41], considerably higher than that of Pt. Its high conductivity is owing to its distinctive Nb-frameworks and graphene-like borophene nanosheets. Such characteristics, along with its unique crystal structure, aids transfer of electrons uniformly in all directions through its lattice.

3.2. Electronic and chemical bonding of α-NbB_2 $\{001\}$ surface

The $\{001\}$ surface of α-NbB_2 has been simulated in order to probe the hydrogen evolution reaction activity of diboride α-NbB_2. By cleaving the 3D bulk α-NbB_2 along the z-direction, two distinct terminations, i.e., B- and Nb-terminated α-NbB_2 $\{001\}$ surface are derived as illustrated in Fig. 2(a–b). The derived B- and Nb-terminated surfaces with a supercell of 2×2 and six Nb/B-layers along the z-direction are considered. In the optimization process, on both surfaces, the top two Nb and B layers have been completely optimized with no symmetry or direction-related constraints, while the remaining layers have been fixed to represent the bulk part.

Subsequently, the electron localization function analysis has been performed to provide a deeper understanding of the chemical bonding characteristics of the α-NbB_2-terminated Nb/B surfaces by cutting out the planes which involve the Nb–Nb and B–B bonds, as illustrated in Fig. 2(b–c). As is well-known, the electron localization function may be analyzed in terms of a 2D contour plot within an interval between 0 and 1. The area near 1 denotes the existence of covalent or single-pair electrons; the area of about 1/2 denotes a homogenous and uniform electron state; while the area near zero refers to an area with small electron distribution. The wide electron localization function value ranging between 0.75–0.85 achieved across two neighboring B -atoms, as can be seen in Fig. 2(b), signifies the presence of a strongly covalent B–B bond with -type σ-type sp^2-hybridization, similar to that found in graphene-like borophene. Meanwhile, for the metallic bond between Nb-atoms, the electron localization function ranging approximately between 0.3–0.5 appear to be well distributed throughout the surface, thus revealing the “electronic jellium” characteristic of the metallic compounds. Also, the differences in electron localization function around the Nb–B bond are highlighted as illustrated in Fig. S1, which indicates that the bond between Nb- and B-atoms has a pure ionic nature. These results were confirmed with the computed Bader charger analysis, revealing approximately 0.85 $|e|$ is transferred from the Nb-atoms into its surrounding B-atoms. Furthermore, the simulated scanning tunneling microscopy (STM) pattern is computed through DFT calculations for the slice cut through the B–B bond so as to offer a clear guide for further experimental investigations. From Fig. 2(c), one can clearly distinguish the B-terminated α-NbB_2 $\{001\}$ surface, in which the B-atoms are more bright than the Nb-atoms.

The electronic characteristics of the $\alpha-$NbB_2 $\{001\}$ surface, through the projected band structure and the corresponding distributed density of states are shown in Fig. 2(d). One can obviously notice the presence of at least three so-called “Dirac cones” in the vicinity of the Fermi-level E_f, showing the semi-metal behavior of the $\{001\}$ surface as in the case of bulk α-NbB_2 structure. Through the distributed density of state depicted in Fig. 3, it is obvious that the three Dirac bands consist mainly of the p-orbitals of B-atoms and the d-orbitals of Nb-atoms. More accurately, they are derived as a result of the coupling of the px/py/pz orbitals of the B-atoms and the $dz^2/dx^2/dxy/dyz/dxz$ of the Nb-atoms.

We have performed additional electronic band structure calculations using the HSE06 hybrid functional to more accurately check the electronic nature and confirm the existence of Dirac cones. Our results as depicted in Figure S6 of supporting information, confirm the semimetallic behavior of α-NbB_2 $\{001\}$ surface, consistent with our findings as elaborated above. Particularly, the existence of Dirac cones in the band structure indicates the presence of linear dispersion of

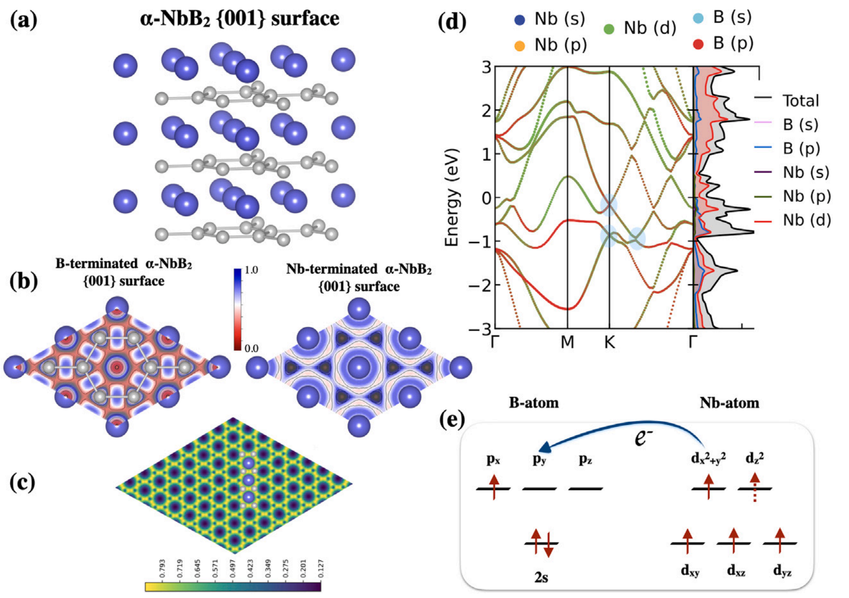

Fig. 2. (a) Schematic representation of the $\alpha-\mathrm{NbB}_2$ {001} surface with (b) the electron localization function by cutting out the planes which involve the Nb–Nb and B–B bonds and (c) the simulated scanning tunneling microscope image of the B-terminated surface. (d) The projected electronic band structure along with the corresponding resolved electronic density of states of $\alpha-\mathrm{NbB}_2$ {001} surface. The energy at the Fermi level was set to zero and the shadow blue-light circles denote the Dirac cone near the Fermi level. (e) schematic illustration of d–sp orbital hybridization. (For interpretation of the references to color in this figure legend, the reader is referred to the web version of this article.)

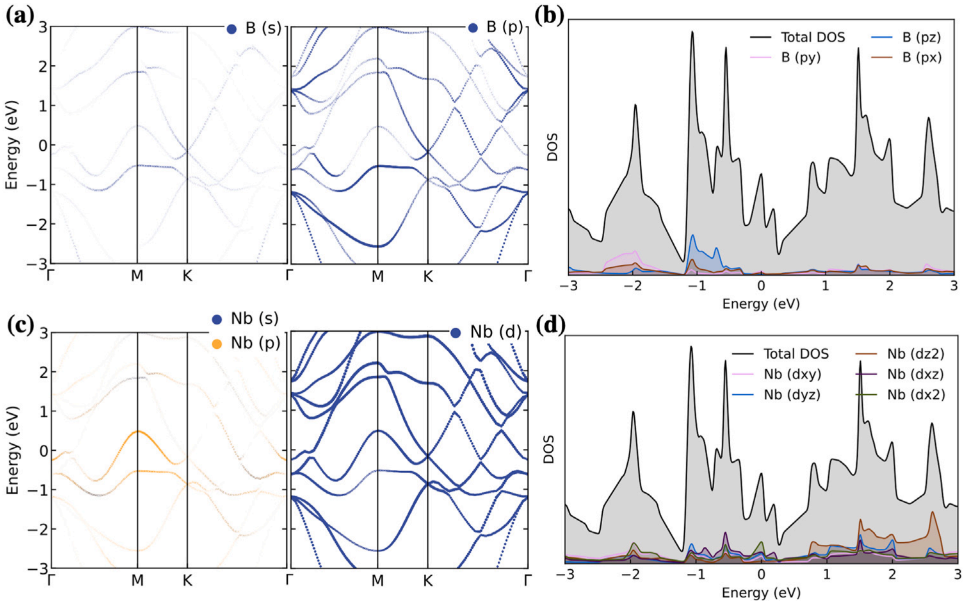

Fig. 3. Projected band structures and orbital-resolved density of state around Fermi level based on PBE calculations for (a,b) B atom and (c,d) Nb atom. The size of colorful dots is proportional to the different orbitals' contributions to the wave function. The energy at the Fermi level was set to zero. (For interpretation of the references to color in this figure legend, the reader is referred to the web version of this article.)

electronic states near the Fermi level. The HSE06 hybrid functional [42,43], which includes a fraction of exact exchange, is well-known and proven to provide a more accurate description of electronic properties than PBE-GGA methods, particularly for strongly correlated systems. Therefore, the use of HSE06 provides additional confirmation and strengthens our conclusions regarding the semi-metallic behavior of α-NbB_2 {001} surface.

To investigate the thermal and dynamic stability of α-NbB_2 {001} surface, we performed Density Functional Perturbation Theory (DFPT) calculations [44,45] to obtain the phonon spectrum and confirm the dynamical stability. The phonon dispersion analysis illustrated in Fig. 4(a), revealed no imaginary frequencies in the spectrum, indicating that the structures are dynamically stable. In addition, we carried out ab-initio molecular dynamics simulations (AIMD) [46,47] to further validate the stability of α-NbB_2 {001} surface at finite temperatures of about 300 and 1000 K (See Fig. 4(b,c,d)). The simulations demonstrated that the structure remains stable and maintains its structural integrity even at elevated temperatures of about 1000 K, suggesting their potential for practical applications. Importantly, the α-NbB_2 {001} surface studied in this work has been previously experimentally synthesized [25,48–50], and we compared structural properties obtained within our study with experimental results to ensure the accuracy and reliability of our calculations. The combination of phonon dispersion analysis and AIMD simulations thus provided rigorous proof of the stability of the surface under different thermal conditions, thereby confirming their suitability for practical applications.

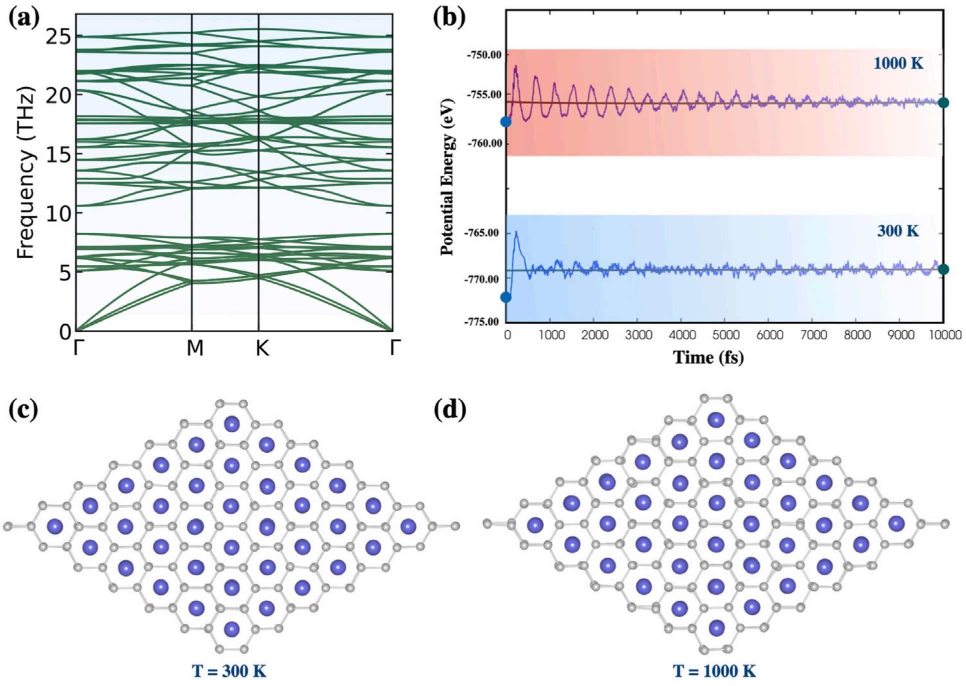

Fig. 4. (a) Calculated phonon spectra of α-NbB$_2$ {001} surface. (b-d) The variation of the potential energy with corresponding top-snapshots of large supercell α-NbB$_2$ {001} surface obtained from AIMD simulations between 0 and 10 ps at 300 K and 1000 K.

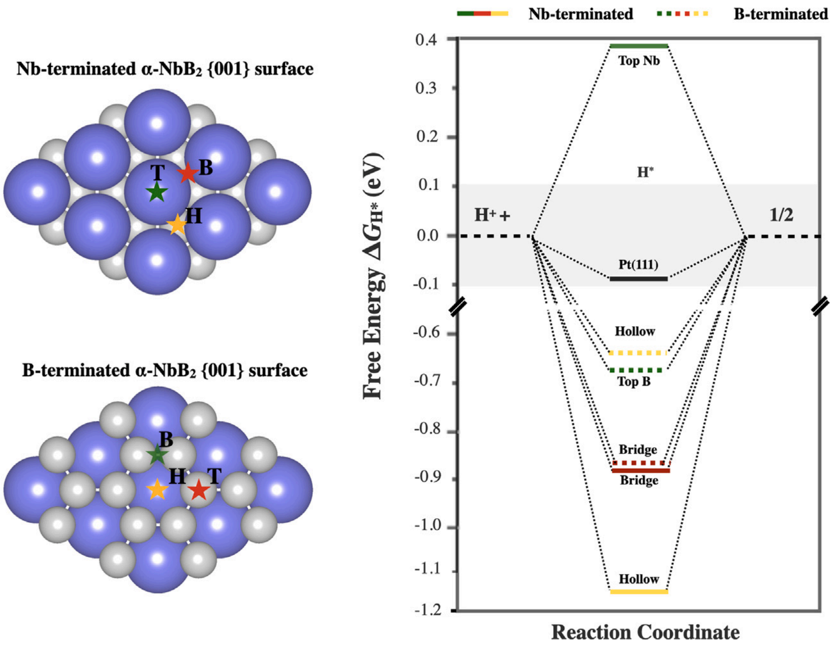

Fig. 5. Different active H* binding sites on Nb- and B-terminated $\alpha-\mathrm{NbB}_2$ {001} surfaces and their corresponding HER free energy diagrams.

3.3. Hydrogen evolution reaction activity on α-NbB$_2$ {001} surface

Electrocatalytic activity of both Nb- and B-terminated $\alpha-\mathrm{NbB}_2$ {001} surface with respect to hydrogen evolution reaction are evaluated and presented in this section. The computed Gibbs free energy (ΔG_{H^*}) at a chosen active site is commonly considered as a robust determinant of the catalytic activity of that particular site relative to hydrogen evolution reaction, where a smaller absolute value of ΔG_{H^*} typically indicates a more active catalyst [11,51].

From the previously conducted studies on the active sites of the HER, it is demonstrated that the active sites in the group-VI transition metal dichalcogenides MX$_2$ (e.g., NbS$_2$, FeS$_2$ and MoS$_2$) [52–57], that are mainly involved in the catalytic process were determined through the catalytic activities of the HER with respect to the respective {001}-surface. As a means of further comparison, the HER activity on the α-NbB$_2$ {001} surface with two terminations as outlined above, i.e., Nb- and B-terminated surface has been investigated within the framework of this study. The HER Gibbs free energy ΔG_{H^*} has been derived on various potential active H* binding sites on Nb- and B-terminated α-NbB$_2$ {001} surface, as illustrated in Fig. 5. It can be clearly noticed that there are three active H* binding sites, namely T- (Top of the Nb-atom), B- (Bridge Nb–Nb bond), and H-site (Hollow site) on the Nb-terminated α-NbB$_2$ {001} surface, and that all of these three potential sites demonstrate catalytic activity for HER, of which their ΔG_{H^*} are

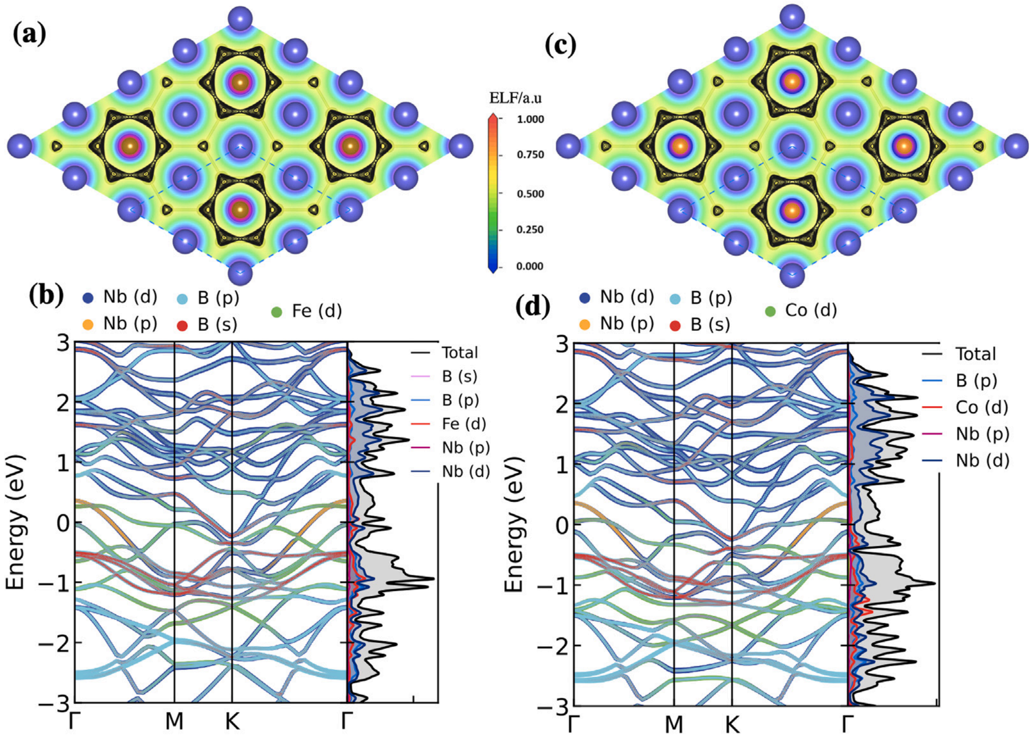

Fig. 6. 2D Contour plot of electron location function and projected band structure of Nb-terminated (a–b) Fe- and (c–d) Co-NbB$_2$ {001} surface, respectively.

respectively found to be about 0.393, −0.897, and −1.151 eV. On the other hand, on the B-terminated α-NbB$_2$ {001} surface, the H* can be potentially adsorbed on the top of the B-atom (T), bridge B–B bond (B), and hollow site (H), with free energy ΔG_{H^*} of about −0.673, −0.889, and −0.647 eV, respectively, indicating their low catalytic activity for HER. Such results provide clear evidence suggesting that the Nb-terminated α-NbB$_2$ {001} surface ought to provide a suitable and optimal HER catalytic activity. Therefore the Nb-terminated {001} surface will be taken as a basis for further research on the strategies to boost the HER activity.

3.4. Hydrogen evolution reaction activity on Fe/Co-NbB$_2$ {001} surface

With the aim of improving the HER electrocatalytic performance, we separately considered Fe and Co doping on the Nb-terminated α-NbB$_2$ {001} surface. To determine the position of the doping atoms, we substituted the Nb atom with the Fe/Co atom on the surface and then optimized the system by minimizing the total energy. The resulting doped surfaces are referred to as Fe/Co-NbB$_2$ {001} surfaces, as shown in Figs. 6(a,c) and 7 with Nb- and B-terminated surfaces, and we evaluated their effectiveness for improving HER electrocatalytic performance as an optimized scheme. Furthermore, as can be clearly seen in Fig. 6(a–d) and Fig. S1 of supporting information, under Fe/Co doping, the relative electron density has been lowered, and also the surface charge has been re-distributed, which can be explained by the relative displacement of the Nb 4d orbital towards the Fermi level, leading to the further lowering of the adsorption-free energy of hydrogen. Accordingly, a covalently Fe/Co-doped NbB$_2$ {001} surface with an Nb-termination is expected to significantly boost the catalytic performance.

As in the case of pure α-NbB$_2$ {001} surfaces, different stable H* binding sites for the Nb-terminated surface on Fe/Co-NbB$_2$ {001} include two top sites (marked $T_{Fe/Co}$ and T_{Nb}), hollow site (H) and two bridge sites characterized Nb–Nb (B$_2$) and Nb–Fe/Co (B$_1$), and the B-terminated of Fe/Co-NbB$_2$ {001} surface comprises of one B–B bridge site (B), top site of B-atom (T), and a hollow site (H) (see the schematic view in Fig. 7). A very optimum HER catalyst displaying optimal HER performance should have a ΔG_{H^*} value close to zero as stated above. Among all the active sites investigated, the Gibbs free energy of the T_{Nb}-site in Fe/Co-NbB$_2$ {001} is 0.264/0.278 eV, which is closer to zero than the Gibbs free energy of the $T_{Fe/Co}$-site (ΔG_{H^*} = −0.542/−0.332 eV) and B2 site (ΔG_{H^*} = −0.663/−0.501 eV), showing a more increased catalytic activity from the thermodynamic perspective. On the other hand, the B-terminated surface exhibits a slightly lower Gibbs free energy of about −0.712/−0.579 eV on the top site of Fe/Co-NbB2 {001} surface.

Additionally, the synergetic effect of Fe/Co doping and an external transverse electric field ranging between 0.05 and 0.55 V/Å on the electrocatalytic activity has been probed in order to boost the HER activity on the Nb-terminated Fe/Co-NbB$_2$ {001} surface. It can be clearly observed how applying a transverse electric field considerably boosts HER activity, as depicted in Fig. 8. The presence of an effective external electric field of 0.30 to 0.45 V/Å can advantageously improve the HER process, with a Gibbs free energy of hydrogen adsorption reaching the catalyst's optimal threshold $\Delta G_{H^*} \leq \pm 0.10$ eV. These results reveal that the Fe and Co covalent doping α-NbB$_2$ {001} surface under an average value of the external electric field would provide a very optimal HER activity.

3.5. Steric effect on the HER activity during hydrogen coverage

Next, we have examined the ΔG_{H^*} with respect to the varying hydrogen concentration (θ_{H^*}) on the Nb-terminated {001} surface of $\alpha-$NbB$_2$ and Fe/Co-NbB$_2$. For the sake of comparison, the ΔG_{H^*} at the respective hydrogen coverage on the Pt (111) surface is correspondingly examined, as it is the most common model surface of Pt that has been extensively investigated for this purpose [58]. Throughout our study, to provide an analogous description to the widely studied Pt(111) surface, ΔG_{H^*} is characterized by the Eq. (4). Furthermore, the hydrogen catalytic stability is described through the hydrogen chemisorption energy ΔG_{H^*} as given in Eq. (5).

From the above description of the hydrogen coverage θ_H^* on Nb-terminated {001} surface, it can be concluded that the hollow (H) and

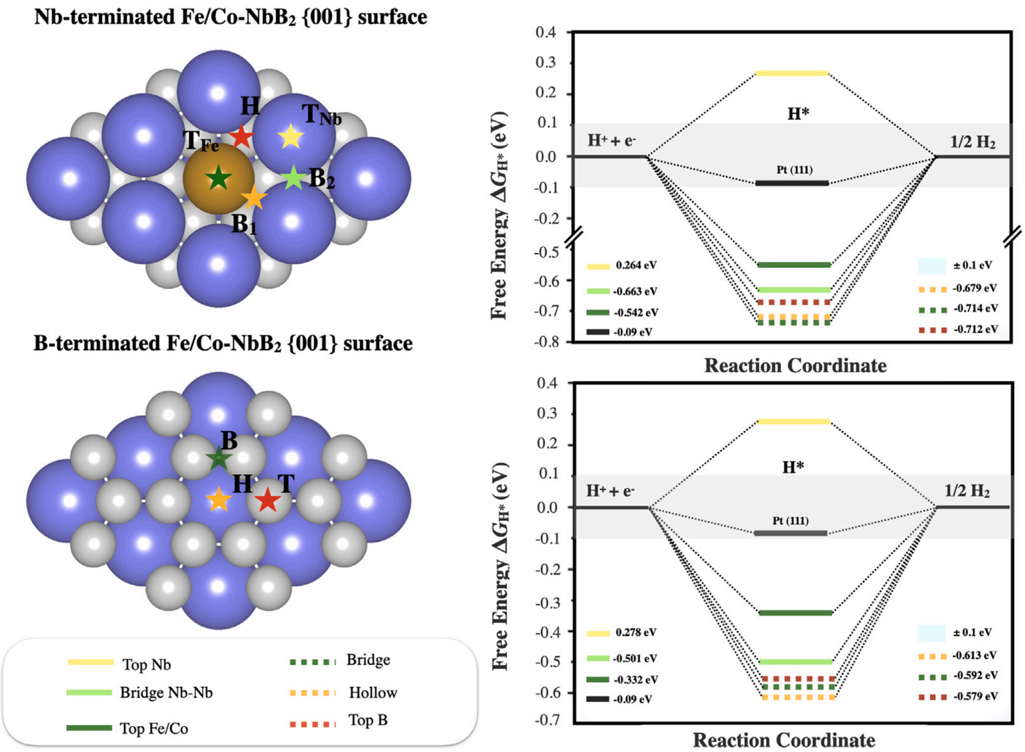

Fig. 7. Schematic view of distinct active H* binding sites on Nb- and B-terminated Fe/Co-NbB$_2$ {001} surface and their corresponding HER free energy diagrams. Hydrogen is unstable in both H- and B$_1$-site of the Nb-terminated surface and optimizes to T$_{Nb/Fe/Co}$ site.

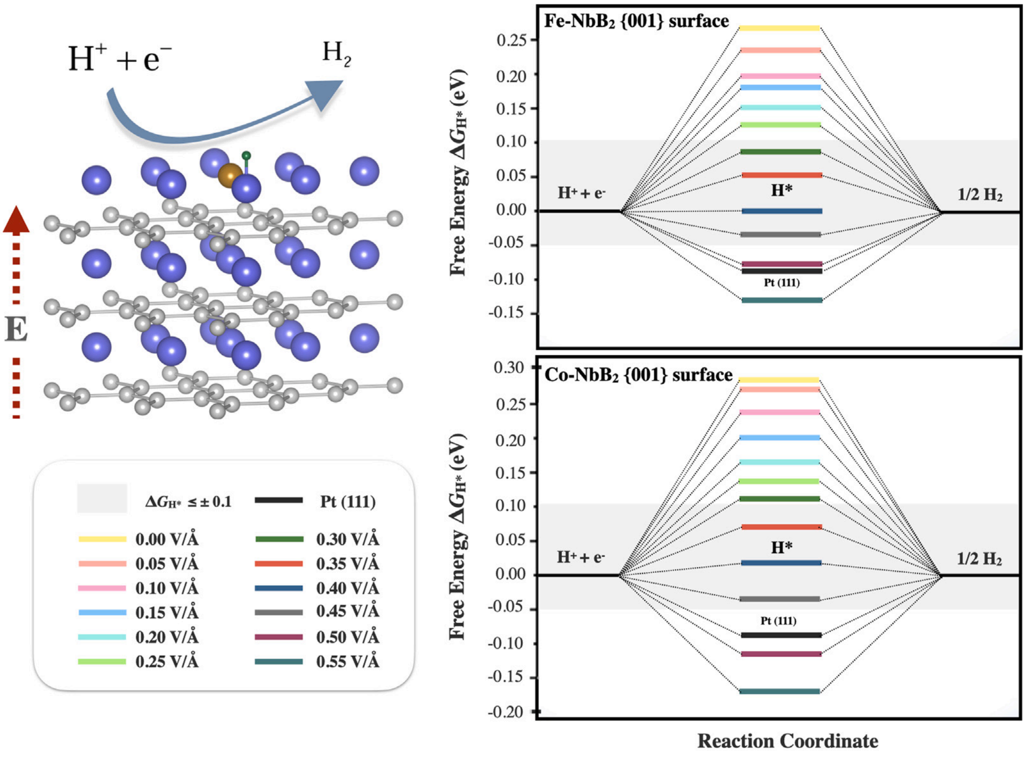

Fig. 8. The effect of the external transverse electric field ranging from 0.0 V/Å to 0.55 V/Å on Gibbs free energy in the case of Nb-terminated Fe/Co-NbB$_2$ {001} surface.

Nb–Nb bridge sites show the strongest interaction with H* in the case of α-NbB$_2$. Therefore, when the hydrogen coverage is small with a θ_{H*} between 0 and 1, hydrogen initially has been found to be adsorbed on the H-sites on the Nb-terminated {001} surface of $\alpha - \text{NbB}_2$. Once the hydrogen coverage rises above $\theta_{H*} = 1–2$, hydrogen then moves to occupy the top of the Nb-atoms, instead of staying on the initial active

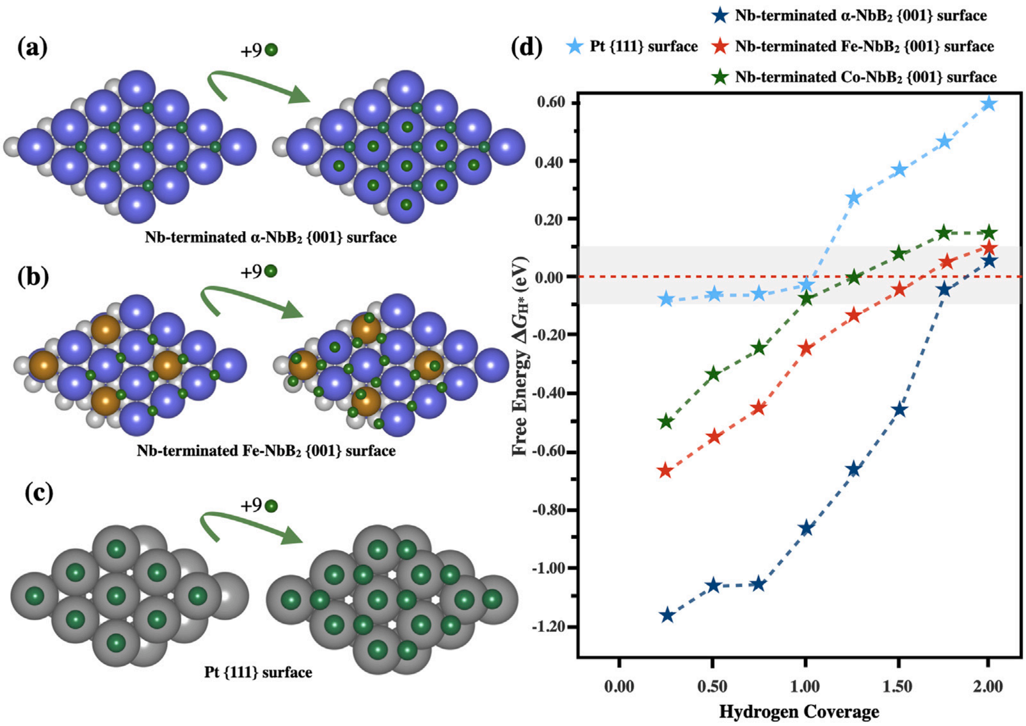

Fig. 9. The fully optimized structures of hydrogen adsorbed on (a) Nb-terminated {111} surface of α-NbB_2, (b) Nb-terminated {001} surface of Fe-NbB_2, and (c) Pt {001} surface at two different hydrogen coverage. (d) Their corresponding variation in hydrogen chemisorption energy ΔG_{H^*} as a function of hydrogen coverage θ_{H^*}.

sites. Likewise, it is confirmed that the B_2-site on the Nb-terminated {001} surface of Fe/Co-NbB_2 has the highest interaction with hydrogen. As a result, it initially occupies the B_2-site for up to $\theta_{H^*} = 1$ hydrogen coverage, and subsequently, moves to other active sites for θ_{H^*} from 1 to 2.

As illustrated in Fig. 9, upon the rise of hydrogen coverage θ_{H^*} from 0 to 1, the Gibbs free energy fluctuates smoothly within the above-mentioned coverage range of −1.159 to −0.921 eV for the pristine Nb-terminated {001} surface of α-NbB_2, while the Gibbs free energy linearly decreases throughout the range of −0.681/−0.501 to −0.241/−0.097 eV for the Nb-terminated {001} surface of Fe/Co-NbB_2. From these findings, it can be concluded that within a narrow interval up to $\theta_{H^*} = 1$, the pristine and Fe/Co-doped α-NbB_2 yield a lesser number of HER-active catalytic sites compared to the Pt{111} surface, owing to the fact that the Gibbs free energy for Pt{001} surface are in the catalyst's optimal threshold $\Delta G_{H^*} \leq \pm 0.10$ eV. Nevertheless, it is shown that the increase of θ_{H^*} leads to poor adsorption of hydrogen on the Pt{111} surface, resulting in a significant increase of ΔG_{H^*} up to 0.579 eV at the highest hydrogen concentration, which can be explained by the high steric effect once the hydrogen coverage is greater than 1 i.e, $\theta_{H^*} > 1$. Thus, our above computational findings strongly reveal that both Nb-terminated {001} surface of α-NbB_2 and Fe/Co-NbB_2 ought to display a large density of high-efficiency HER-catalytic sites.

4. Conclusion

In conclusion, we have systematically investigated electronic properties and chemical bonding of α-NbB_2 {001} surface and Fe/Co covalent doping α-NbB_2 {001} surfaces through first-principles calculations. Both Nb- and B-terminated Fe/Co-NbB_2 {001} surfaces have been extensively explored as promising catalysts for HER from a thermodynamic point of view via free energy corresponding to hydrogen chemisorption. Fe/Co-NbB_2 {001} surface shows outstanding HER activity with a lower H^*-adsorption energy ΔG_{H^*} of about 0.264/0.278 eV. Additionally, the H^*-adsorption free energy of Nb-terminated Fe/Co-NbB_2 {001} surface catalyst reaches very low values in the range of $\Delta G_{H^*} \leq \pm 0.10$ eV in the presence of an external electric field, which is the interval of optimal catalysts. Also, the synergistic effect of hydrogen coverage has been explored and revealed that Nb-terminated Fe/Co-NbB_2 {001} exhibit an increased catalytic activity for HER for a large hydrogen coverage. Thus, the results of this study expand not only the understanding of the effect of covalent doping on the enhancement of the overpotential related to the HER performance but also offers a new perspective for designing cost-effective transition metal boride-based catalysts.

CRediT authorship contribution statement

Nabil Khossossi: Conceptualization, Data curation, Methodology, Formal analysis, Validation, Visualization, Writing – original draft, Review & editing. **Amitava Banerjee:** Validation, Visualization, Writing – review & editing. **Poulumi Dey:** Conceptualization, Funding acquisition, Project administration, Resources, Software, Supervision, Validation.

Declaration of competing interest

The authors declare that they have no known competing financial interests or personal relationships that could have appeared to influence the work reported in this paper.

Data availability

No data was used for the research described in the article.

Acknowledgments

This work was sponsored by Nederlandse Organisatie voor Wetenschappelijk Onderzoek (The Netherlands Organization for Scientific Research, NWO) domain Science for the use of supercomputer facilities.

Appendix A. Supplementary data

Supplementary material related to this article can be found online at https://doi.org/10.1016/j.surfin.2023.102972.

References

[1] B. Ghorbani, S. Zendehboudi, Z.A. Afrouzi, Multi-objective optimization of an innovative integrated system for production and storage of hydrogen with net-zero carbon emissions, Energy Convers. Manage. 276 (2023) 116506.

[2] N. Khossossi, Y. Benhouria, S.R. Naqvi, P.K. Panda, I. Essaoudi, A. Ainane, R. Ahuja, Hydrogen storage characteristics of Li and Na decorated 2D boron phosphide, Sustain. Energy Fuels 4 (9) (2020) 4538–4546.

[3] P. Habibi, T.J. Vlugt, P. Dey, O.A. Moultos, Reversible hydrogen storage in metal-decorated honeycomb borophene oxide, ACS Appl. Mater. Interfaces 13 (36) (2021) 43233–43240.

[4] W. Liu, L. Sun, Z. Li, M. Fujii, Y. Geng, L. Dong, T. Fujita, Trends and future challenges in hydrogen production and storage research, Environ. Sci. Pollut. Res. 27 (2020) 31092–31104.

[5] A. Li, Y. Sun, T. Yao, H. Han, Earth-abundant transition-metal-based electrocatalysts for water electrolysis to produce renewable hydrogen, Chem. Eur. J. 24 (69) (2018) 18334–18355.

[6] M.A. Khan, H. Zhao, W. Zou, Z. Chen, W. Cao, J. Fang, J. Xu, L. Zhang, J. Zhang, Recent progresses in electrocatalysts for water electrolysis, Electrochem. Energy Rev. 1 (2018) 483–530.

[7] A. Banerjee, S. Chakraborty, N.K. Jena, R. Ahuja, Scrupulous probing of bifunctional catalytic activity of borophene monolayer: mapping reaction coordinate with charge transfer, ACS Appl. Energy Mater. 1 (8) (2018) 3571–3576.

[8] B. You, Y. Sun, Innovative strategies for electrocatalytic water splitting, Acc. Chem. Res. 51 (7) (2018) 1571–1580.

[9] A.T. Hoang, A. Pandey, W.-H. Chen, S.F. Ahmed, S. Nižžetic, K.H. Ng, Z. Said, X.Q. Duong, U. Agçbulut, H. Hadiyanto, et al., Hydrogen production by water splitting with support of metal and carbon-based photocatalysts, ACS Sustain. Chem. Eng. (2023).

[10] X. Yang, A. Banerjee, R. Ahuja, Probing the active sites of newly predicted stable Janus scandium dichalcogenides for photocatalytic water-splitting, Catalysis Sci. Technol. 9 (18) (2019) 4981–4989.

[11] Z. Haman, N. Khossossi, M. Kibbou, I. Bouziani, D. Singh, I. Essaoudi, A. Ainane, R. Ahuja, Janus Aluminum Oxysulfide Al2OS: A promising 2D direct semiconductor photocatalyst with strong visible light harvesting, Appl. Surf. Sci. 589 (2022) 152997.

[12] X. Yang, A. Banerjee, Z. Xu, Z. Wang, R. Ahuja, Interfacial aspect of ZnTe/In 2 te 3 heterostructures as an efficient catalyst for the hydrogen evolution reaction, J. Mater. Chem. A 7 (48) (2019) 27441–27449.

[13] F. Si, W. Wei, M. Li, X. Xie, Q. Gao, X. Cai, S. Zhang, F. Peng, Y. Fang, S. Yang, Natural light driven photovoltaic-electrolysis water splitting with 12.7% solar-to-hydrogen conversion efficiency using a two-electrode system grown with metal foam, J. Power Sources 538 (2022) 231536.

[14] M. Kibbou, Z. Haman, N. Khossossi, D. Singh, I. Essaoudi, A. Ainane, R. Ahuja, Probing the electronic, optical and transport properties of halide double perovskites Rb2InSb (Cl, Br) 6 for solar cells and thermoelectric applications, J. Solid State Chem. 312 (2022) 123262.

[15] N. Khossossi, D. Singh, W. Luo, R. Ahuja, Strong optical excitation and high thermoelectric performance in 2D holey-phosphorene monolayer, Energy Technol. 10 (10) (2022) 2200400.

[16] S.T. Renosto, R. Lang, E. Diez, L.E. Corrêa, M. da Luz, Z. Fisk, A.J.d.S. Machado, Evidence of unconventional superconductivity in the Ni-doped NbB2 system, J. Alloys Compd. 787 (2019) 414–422.

[17] J. Ran, M. Jaroniec, S.-Z. Qiao, Cocatalysts in semiconductor-based photocatalytic CO2 reduction: achievements, challenges, and opportunities, Adv. Mater. 30 (7) (2018) 1704649.

[18] H. Sun, J. Meng, L. Jiao, F. Cheng, J. Chen, A review of transition-metal boride/phosphide-based materials for catalytic hydrogen generation from hydrolysis of boron-hydrides, Inorg. Chem. Front. 5 (4) (2018) 760–772.

[19] S. Carenco, D. Portehault, C. Boissiere, N. Mezailles, C. Sanchez, Nanoscaled metal borides and phosphides: recent developments and perspectives, Chem. Rev. 113 (10) (2013) 7981–8065.

[20] S. Gupta, M.K. Patel, A. Miotello, N. Patel, Metal boride-based catalysts for electrochemical water-splitting: A review, Adv. Funct. Mater. 30 (1) (2020) 1906481.

[21] L. Shi, P. Wang, Q. Wang, X. Ren, F. Ichihara, W. Zhou, H. Zhang, Y. Izumi, B. Cao, S. Wang, et al., Efficient photocatalytic CO 2 reduction mediated by transitional metal borides: metal site-dependent activity and selectivity, J. Mater. Chem. A 8 (41) (2020) 21833–21841.

[22] Y. Zhao, L. Zhang, J. Xiang, X. Chen, C. Zhu, K. Wang, J. Li, H. Ma, X. Song, L. Wang, et al., Topological tailoring-induced Dirac cone in ultrathin niobium diboride nanosheets for electrocatalytic sulfur reduction reaction, Mater. Today Phys. 32 (2023) 101029.

[23] X. Li, J. Huang, L. Feng, D. He, Z. Liu, G. Li, N. Zhang, Y. Feng, L. Cao, Molybdenum and cobalt co-doped VC nanoparticles encapsulated in nanocarbon as efficient electrocatalysts for the hydrogen evolution reaction, Inorg. Chem. Front. 9 (5) (2022) 870–878.

[24] N. Patel, G. Guella, A. Kale, A. Miotello, B. Patton, C. Zanchetta, L. Mirenghi, P. Rotolo, Thin films of Co–B prepared by pulsed laser deposition as efficient catalysts in hydrogen producing reactions, Appl. Catal. A 323 (2007) 18–24.

[25] J. Wang, C. Liu, K. Miao, K. Zhang, W. Zheng, C. Chen, Macroscale robust superlubricity on metallic NbB2, Adv. Sci. 9 (13) (2022) 2103815.

[26] J.K. Nø rskov, T. Bligaard, A. Logadottir, J. Kitchin, J.G. Chen, S. Pandelov, U. Stimming, Trends in the exchange current for hydrogen evolution, J. Electrochem. Soc. 152 (3) (2005) J23–J26.

[27] N. Marković, B. Grgur, P.N. Ross, Temperature-dependent hydrogen electrochemistry on platinum low-index single-crystal surfaces in acid solutions, J. Phys. Chem. B 101 (27) (1997) 5405–5413.

[28] G. Kresse, J. Furthmüller, Efficient iterative schemes for ab initio total-energy calculations using a plane-wave basis set, Phys. Rev. B 54 (16) (1996) 11169.

[29] J.P. Perdew, K. Burke, M. Ernzerhof, Generalized gradient approximation made simple, Phys. Rev. Lett. 77 (18) (1996) 3865.

[30] S. Grimme, J. Antony, S. Ehrlich, H. Krieg, A consistent and accurate ab initio parametrization of density functional dispersion correction (DFT-D) for the 94 elements H-Pu, J. Chem. Phys. 132 (15) (2010) 154104.

[31] H.J. Monkhorst, J.D. Pack, Special points for Brillouin-zone integrations, Phys. Rev. B 13 (12) (1976) 5188.

[32] P.E. Blöchl, Projector augmented-wave method, Phys. Rev. B 50 (24) (1994) 17953.

[33] A. Gupta, V. Singhal, O. Pandey, Facile in-situ synthesis of NbB2 nanoparticles at low temperature, J. Alloys Compd. 736 (2018) 306–313.

[34] A.A. Shokati, N. Parvin, N. Sabzianpour, M. Shokati, A. Hemmati, In situ synthesis of NiAl–NbB2 composite powder through combustion synthesis, J. Alloys Compd. 549 (2013) 141–146.

[35] S. Jin, P. Shen, Y. Li, D. Zhou, Q. Jiang, Synthesis of spherical NbB 2- x particles by controlling the stoichiometry, Cryst. Eng. Comm. 14 (6) (2012) 1925–1928.

[36] P. Vajeeston, P. Ravindran, C. Ravi, R. Asokamani, Electronic structure, bonding, and ground-state properties of AlB 2-type transition-metal diborides, Phys. Rev. B 63 (4) (2001) 045115.

[37] A. Islam, A. Sikder, F. Islam, NbB2: a density functional study, Phys. Lett. A 350 (3–4) (2006) 288–292.

[38] E. Regalado, R. Escamilla, Elastic properties of superconducting NbB2+ x obtained from first-principles calculations, J. Phys.: Condens. Matter 19 (37) (2007) 376209.

[39] K. Sairam, J. Sonber, T.C. Murthy, C. Subramanian, R. Fotedar, R. Hubli, Reaction spark plasma sintering of niobium diboride, Int. J. Refractory Metals Hard Mater. 43 (2014) 259–262.

[40] X. Wang, Y. Yang, S. Jia, Y. Wang, Y. Ma, Y. Cui, X. Wang, W. Sun, L. Wang, In-situ synthesis, microstructure, and properties of NbB2-NbC-Al2O3 composite coatings by plasma spraying, J. Adv. Ceramics 11 (8) (2022) 1263–1278.

[41] C. Yeh, W. Chen, Preparation of niobium borides NbB and NbB2 by self-propagating combustion synthesis, J. Alloys Compd. 420 (1–2) (2006) 111–116.

[42] A.V. Krukau, O.A. Vydrov, A.F. Izmaylov, G.E. Scuseria, Influence of the exchange screening parameter on the performance of screened hybrid functionals, J. Chem. Phys. 125 (22) (2006) 224106.

[43] L. Schimka, J. Harl, G. Kresse, Improved hybrid functional for solids: The HSEsol functional, J. Chem. Phys. 134 (2) (2011) 024116.

[44] K. Refson, P.R. Tulip, S.J. Clark, Variational density-functional perturbation theory for dielectrics and lattice dynamics, Phys. Rev. B 73 (15) (2006) 155114.

[45] S. Baroni, S. De Gironcoli, A. Dal Corso, P. Giannozzi, Phonons and related crystal properties from density-functional perturbation theory, Rev. Modern Phys. 73 (2) (2001) 515.

[46] D. Marx, J. Hutter, Ab initio molecular dynamics: Theory and implementation, Mod. Methods Algorithms Quantum Chem. 1 (301–449) (2000) 141.

[47] M.E. Tuckerman, Ab initio molecular dynamics: basic concepts, current trends and novel applications, J. Phys.: Condens. Matter 14 (50) (2002) R1297.

[48] N. Nedfors, O. Tengstrand, J. Lu, P. Eklund, P.O. Persson, L. Hultman, U. Jansson, Superhard NbB2- x thin films deposited by dc magnetron sputtering, Surf. Coat. Technol. 257 (2014) 295–300.

[49] T. Aizawa, W. Hayami, S. Otani, Surface phonon dispersion of ZrB 2 (0001) and NbB 2 (0001), Phys. Rev. B 65 (2) (2001) 024303.

[50] E. Wuchina, E. Opila, M. Opeka, B. Fahrenholtz, I. Talmy, UHTCs: ultra-high temperature ceramic materials for extreme environment applications, Electrochem. Soc. Interface 16 (4) (2007) 30.

[51] B. Hinnemann, P.G. Moses, J. Bonde, K.P. Jø rgensen, J.H. Nielsen, S. Horch, I. Chorkendorff, J.K. Nø rskov, Biomimetic hydrogen evolution: MoS2 nanoparticles as catalyst for hydrogen evolution, J. Am. Chem. Soc. 127 (15) (2005) 5308–5309.

[52] D. Gopalakrishnan, A. Lee, N.K. Thangavel, L.M.R. Arava, Facile synthesis of electrocatalytically active NbS 2 nanoflakes for an enhanced hydrogen evolution reaction (HER), Sustain. Energy Fuels 2 (1) (2018) 96–102.

[53] Y. Li, H. Wang, L. Xie, Y. Liang, G. Hong, H. Dai, MoS2 nanoparticles grown on graphene: an advanced catalyst for the hydrogen evolution reaction, J. Am. Chem. Soc. 133 (19) (2011) 7296–7299.

[54] L. Najafi, S. Bellani, R. Oropesa-Nuñez, B. Martín-García, M. Prato, V. Mazánek, D. Debellis, S. Lauciello, R. Brescia, Z. Sofer, et al., Niobium disulphide (NbS 2)-based (heterogeneous) electrocatalysts for an efficient hydrogen evolution reaction, J. Mater. Chem. A 7 (44) (2019) 25593–25608.

[55] Y. Zhao, Z. Zhang, J. Li, X. Li, T. Liu, Structural engineering of ultrathin vertical NbS2 on carbon cloth by chemical vapor deposition for hydrogen evolution reaction, Functional Mater. Lett. 15 (03) (2022) 2251024.

[56] M.S. Faber, M.A. Lukowski, Q. Ding, N.S. Kaiser, S. Jin, Earth-abundant metal pyrites (FeS2, CoS2, NiS2, and their alloys) for highly efficient hydrogen evolution and polysulfide reduction electrocatalysis, J. Phys. Chem. C 118 (37) (2014) 21347–21356.

[57] X. Huang, H. Xu, D. Cao, D. Cheng, Interface construction of P-substituted MoS2 as efficient and robust electrocatalyst for alkaline hydrogen evolution reaction, Nano Energy 78 (2020) 105253.

[58] E. Skúlason, V. Tripkovic, M.E. Björketun, S. Gudmundsdóttir, G. Karlberg, J. Rossmeisl, T. Bligaard, H. Jónsson, J.K. Nø rskov, Modeling the electrochemical hydrogen oxidation and evolution reactions on the basis of density functional theory calculations, J. Phys. Chem. C 114 (42) (2010) 18182–18197.